Nanoscale

RSC Publishing

PAPER

Nanosize SnO_2 confined in the porous shells of carbon cages for kinetically efficient and long-term lithium storage†

Cite this: *Nanoscale*, 2013, **5**, 1576

Guangmin Zhou,[a] Da-Wei Wang,[b] Lu Li,[a] Na Li,[a] Feng Li*[a] and Hui-Ming Cheng[a]

Received 5th November 2012
Accepted 12th December 2012

DOI: 10.1039/c2nr33482h

www.rsc.org/nanoscale

We explore a hybrid material consisting of SnO_2 nanoparticles (NPs) embedded in the porous shells of carbon cages (SnO_2–PSCC). The hybrid material exhibits improved kinetics of lithiation–delithiation and high reversible capacity, and excellent cyclic stability without capacity loss over 100 cycles at 500 mA g^{-1} with a coulombic efficiency close to 100% after the initial cycle. This can be ascribed to the high electrical conductivity, the hierarchical porosity and the confinement effect of the PSCC on the volume change of SnO_2 NPs. The material has a large reversible capacity of 460 mA h g^{-1} at a high current density of 5 A g^{-1} due to a short ion diffusion length in the bulk and large number of inter-pore ion transport channels. These results provide insight into improving the lithium storage performance of SnO_2 by facilitating the reaction kinetics and indicate that this hybrid material has great potential for use in high-rate and durable lithium ion batteries.

1 Introduction

Lithium ion batteries (LIBs) with a high capacity, fast charge–discharge and long cyclic life are of great importance as power sources for portable electronic devices and hybrid/electric vehicles.[1–3] To date, graphite is the most commonly used anode material using an intercalation reaction for lithium storage. However, the limited theoretical capacity of 372 mA h g^{-1} and low interlayer diffusion coefficient of graphite anodes restrict the development of high energy and high power LIBs.[4,5] In recent years, SnO_2-based anode materials have attracted increasing interest due to their high theoretical gravimetric capacity based on an alloying reaction which is two to three times that of a commercial graphite anode in LIBs.[6–9] Moreover, the low lithiation–delithiation potentials of SnO_2 (0.01 V *vs.* Li/Li^+ for Li–Sn alloying reaction) provide an opportunity to obtain high voltage and high energy LIBs.[10] Nonetheless, the practical implementation of SnO_2 to LIBs is greatly hampered by its severe volume expansion and contraction (~300%) during the charge–discharge process, leading to poor cyclic stability due to the pulverization and loss of electrical contact in the electrode.[11]

Many strategies have been proposed to overcome these issues. One of the most studied approaches is to reduce the particle size of the oxides to nanometer scale to alleviate the volume change and simultaneously shortening the ion diffusion length.[10,12] However, the agglomeration of oxide nanoparticles (NPs) during alloying/de-alloying reactions induces a large stress on the aggregates, causing pulverization and fast capacity loss.[13,14] Designing porous or hollow SnO_2 particles is another widely used strategy to accommodate the volume change and shows a positive effect in improving the diffusion kinetics and cyclic life.[15–19] For instance, SnO_2 hollow spheres,[15] mesoporous SnO_2 microspheres,[16] hollow core–shell SnO_2 mesospheres,[17] porous microspheres of SnO_2 octahedral,[18] and SnO_2 nanoboxes[19] were reported as effective ways to circumvent the pulverization problem. Beside these methods, homogeneously dispersing SnO_2 NPs in a carbon matrix is useful not only for minimizing the agglomeration, but also for accommodating the volume change and reducing the intraparticle resistance. For example, SnO_2-porous carbons,[20,21] SnO_2-carbon nanotubes[22,23] and SnO_2-graphene composites[24,25] have shown improved lithium storage properties. Previous studies mainly focus on the improvement of electrical conductivity and in relaxing the internal stress of SnO_2 associated with lithium insertion/extraction. However, the reaction kinetics and the lithiation–delithiation reversibility of SnO_2 dispersed in a carbon matrix has received less consideration and is worth investigating. The study of reaction kinetics will facilitate the understanding of the reversibility, high rate capability and long-term cyclic stability of the lithiation–delithiation of SnO_2. Moreover, combining SnO_2 with

[a]*Shenyang National Laboratory for Materials Science, Institute of Metal Research, Chinese Academy of Sciences, 72 Wenhua Road, Shenyang 110016, China. E-mail: fli@imr.ac.cn*

[b]*ARC Centre of Excellence for Functional Nanomaterials, Australian Institute for Bioengineering and Nanotechnology, The University of Queensland, St Lucia, Brisbane, QLD 4072, Australia*

† Electronic supplementary information (ESI) available. See DOI: 10.1039/c2nr33482h

high capacity carbonaceous materials to integrate different lithium storage modes is promising.

Recently, we found that porous carbon cages with high electrical conductivity and interconnected pores deliver superior rate and cyclic performance in LIBs, and a higher capacity was obtained through lithium storage in micropores in the shells.[26] Therefore, embedding SnO_2 NPs in the porous shells of the carbon cages (PSCC) should enable one to take advantage of both effects for improving the reaction kinetics of SnO_2, and the lithium storage and thus obtain superior LIB anode performance. Here, we explore the uniform loading of SnO_2 NPs in a PSCC matrix, in which the SnO_2 NPs are confined in the porous shells of PSCC. Our results suggest that the reversible lithiation–delithiation and high rate capacity are due to the improved reaction kinetics while the higher capacity arises from different active sites for lithium storage. As a consequence, an anode comprised of SnO_2 NPs and high ionic/electronic conducting PSCC (SnO_2–PSCC) shows a high capacity, exceptional cyclic performance and high rate capability.

2 Experimental

Synthesis of SnO_2–PSCC hybrid

The preparation of PSCC was described in our previous work.[26] The SnO_2–PSCC hybrid was synthesized by a melting impregnation–hydrolysis–thermal annealing approach (Scheme 1). 100 mg PSCC was mixed with 10 mmol tin(II) chloride dihydrate ($SnCl_2 \cdot 2H_2O$) in an agate mortar to obtain a homogeneous mixture. The mixture was sealed in a 10 ml glass bottle with heat treatment at 80 °C for 12 h in an oven. In this step, $SnCl_2 \cdot 2H_2O$ was melted so that it could impregnate into the pores, and be adsorbed on the exterior/interior surface, of the PSCC. Then the mixture was washed with ethanol to remove the excess $SnCl_2$, followed by de-ionized water to promote the hydrolysis of $SnCl_2$. The mixture of PSCC and hydrolyzate was centrifuged and dried under vacuum at 80 °C for 12 h. Finally, the SnO_2–PSCC hybrid was obtained by further thermal annealing in air at 300 °C for 2 h in a tube furnace.

Synthesis of SnO_2

The synthesis procedure for SnO_2 is the same as that for SnO_2–PSCC hybrid but without adding PSCC.

Materials characterization

X-Ray diffraction (XRD) patterns of the samples were recorded with a Rigaku diffractometer using Cu Kα irradiation. X-Ray photoelectron spectroscopy (XPS) analysis was performed on an ESCALAB 250 instrument with Al Kα radiation (15 kV, 150 W) under a pressure of 4×10^{-8} Pa. Transmission electron microscopy (TEM) and high angle angular dark field-scanning TEM (HAADF-STEM) were performed on a Tecnai F30 (300 kV). Scanning electron microscopy (SEM) was carried out on a FEI Nova NanoSEM 430 at 15 kV. Pore parameters were determined using a Micromeritics ASAP 2020 M at 77 K with liquid nitrogen. Thermogravimetric analyses (TGA) were performed on a NETZSCH STA 449C in air with a heating ramp of 10 °C min^{-1} from room temperature to 1000 °C.

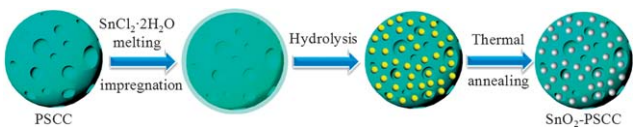

Scheme 1 Schematic of the synthesis of SnO_2–PSCC hybrid by a melting impregnation–hydrolysis–thermal annealing approach.

Electrochemical measurements

The electrochemical properties of the SnO_2–PSCC hybrid and SnO_2 as anode materials were evaluated by a galvanostatic charge–discharge technique. The test electrodes were prepared by mixing 80 wt% active material with 10 wt% conductive carbon black (super P) as a conducting agent and 10 wt% polyvinylidene fluoride (PVDF) dissolved in *N*-methyl-2-pyrrolidone (NMP) as a binder to form a slurry, which was coated onto a copper foil, pressed and dried under vacuum at 120 °C for 12 h. The mass loading of the electrodes was about 2–3 mg per cm^2. 2032-type coin cells were assembled in an argon-filled glove box with the samples as test electrode, metallic lithium as the counter/reference electrode, a mixture of 1 M $LiPF_6$ in ethylene carbonate, dimethyl carbonate and ethylmethyl carbonate (EC–DMC–EMC, 1 : 1 : 1 vol) as the electrolyte, and a Celgard 2400 polypropylene membrane as the separator. Charge–discharge measurements were carried out galvanostatically at different current densities over the voltage range of 0.001 to 3 V (*vs.* Li/Li^+) at various rates using a battery test system (LAND CT2001A, Wuhan Jinnuo Electronics. Ltd.). Cyclic voltammetry (CV) measurements were carried out using a Solartron 1287 electrochemical workstation in the voltage range of 0.001–3.0 V (*vs.* Li^+/Li) at a scan rate of 0.5 mV s^{-1}. Electrochemical impedance spectroscopy (EIS) measurements were carried out after CV measurements by applying a perturbation voltage of 10 mV in the frequency range of 100 kHz to 10 mHz using a Solartron 1287/1260 electrochemical workstation.

3 Results and discussion

The crystallographic structure and elemental composition of the samples obtained were studied by XRD and XPS. The XRD profiles of the SnO_2–PSCC hybrid and SnO_2 are shown in Fig. 1a. All the peaks can be indexed to crystalline rutile SnO_2 (JCPDS no. 41-1445), and the broad diffraction humps indicate the nanosized crystallinity of SnO_2 particles. The particle size of SnO_2 is around 5 nm according to the Scherrer equation. Fig. 1b shows the XPS spectrum of the hybrid, which reveals the presence of carbon, oxygen and tin. The C 1s peak observed at 284.6 eV is related to sp^2-hybridized carbon atoms in the PSCC. The Sn 3d regions with two peaks centered at 494.9 and 486.5 eV (Fig. 1c) are attributed to Sn $3d_{3/2}$ and Sn $3d_{5/2}$, which suggests the (IV) state of Sn, *i.e.* the existence of SnO_2.[7,17,27] The presence of SnO_2 can be further confirmed by the O 1s XPS spectrum (Fig. 1d), which can be deconvoluted into three peaks. The peak at 530.1 eV corresponds to oxygen species in SnO_2, and the other

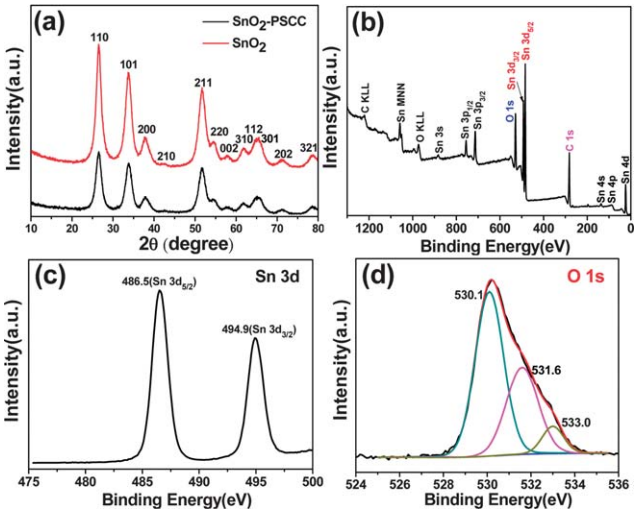

Fig. 1 (a) XRD patterns of the SnO_2–PSCC hybrid and SnO_2. (b) XPS spectrum of the SnO_2–PSCC hybrid. (c) Sn 3d and (d) O 1s XPS spectra of the SnO_2–PSCC hybrid.

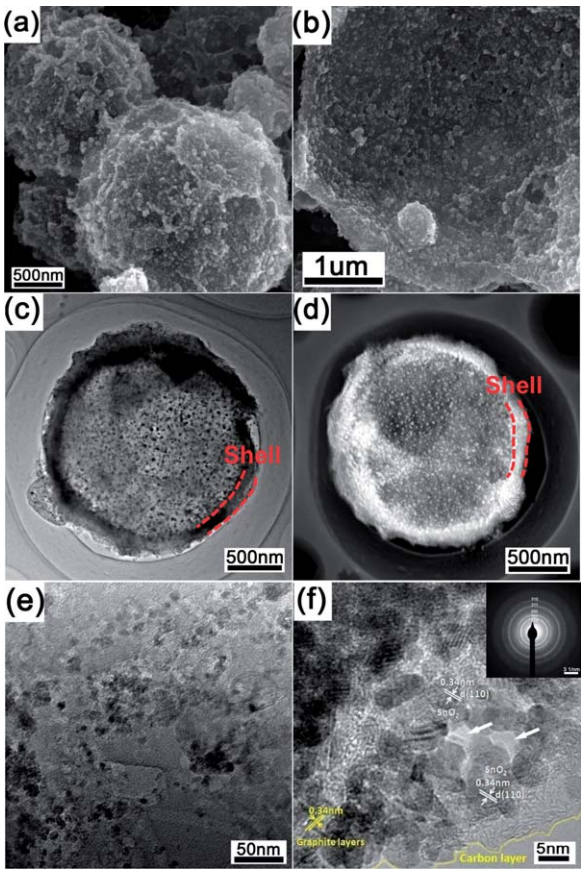

Fig. 2 (a) SEM image of the SnO_2–PSCC hybrid, (b) SEM image of the interior of the SnO_2–PSCC hybrid, (c) TEM and (d) HAADF-STEM images of the SnO_2–PSCC hybrid, (e) TEM image showing that the interconnected pores are partially filled by SnO_2 NPs, (f) HRTEM image of the SnO_2–PSCC hybrid and the corresponding SAED pattern shown in the inset.

two peaks at 531.6 and 533.0 eV are ascribed to the oxygen atoms in C═O groups, C–OH and/or C–O–C groups from PSCC, respectively.[28–30] These polar groups are favorable to the adsorption of precursor ions and the nucleation of SnO_2 on the surface and in the pores of the PSCC.[27,30]

Fig. 2 presents typical SEM and TEM images of the SnO_2–PSCC hybrid material. The diameter of spherical SnO_2–PSCC ranges from 1 to 3 μm with a rough surface which is beneficial for the deposition of foreign substances, and the spheres are uniformly covered by SnO_2 NPs (Fig. 2a). The loading (weight ratio) of SnO_2 in the hybrid was 60.0 wt% determined by TGA as shown in Fig. S1.† A fracture surface of PSCC in Fig. 2b shows a hollow structure and a large number of SnO_2 NPs are homogeneously distributed on its interior surface. The TEM and HAADF-STEM images (Fig. 2c and d) show the uniform deposition of SnO_2 NPs. By comparison, SnO_2 particles prepared in the same conditions without adding PSCC tend to agglomerate, as shown in Fig. S2.† The contrast between the shell and the core (Fig. 2c and d) of the hybrid confirms the hollow structure with a shell thickness of 100–200 nm (marked by the red dotted line). The SnO_2 NPs are firmly attached to PSCC even after ultrasonication treatment that was used to disperse the SnO_2–PSCC hybrid for TEM characterization. This result suggests the strong bonding of these NPs in PSCC which prevents them from becoming detached and moving away. The TEM image (Fig. 2e) reveals that the interconnected pores are partially filled by SnO_2 NPs. Fig. 2f shows a high-resolution TEM (HRTEM) image of the hybrid, in which the average particle size of the SnO_2 is around 5 nm, which is in good agreement with XRD measurements. The adjacent fringe spacing of the aligned lattice fringes was about 0.34 nm, corresponding to the (110) plane of the rutile SnO_2 phase. These NPs locate on the carbon layers (indicated by a dotted yellow line) or inside the pores surrounded by graphitic layers with an interplanar distance of 0.34 nm. It can be clearly seen that the additional voids are formed between individual SnO_2 NPs (marked by white arrowheads). The corresponding selected-area electron diffraction (SAED) pattern of the hybrid is shown in the inset of Fig. 2f. The ring-like character indicates that the SnO_2 NPs are crystalline, and all diffraction rings can be indexed to SnO_2.

Nitrogen adsorption experiments were conducted to evaluate changes in the pore structure caused by incorporation of SnO_2 in the PSCC (Fig. 3a and Table S1†). The isotherms of PSCC are type-IV, which indicates the existence of micropores and mesopores, while negligible pores were observed for SnO_2. After loading with SnO_2, the adsorption amount at a relative pressure below 0.1 decreases, as does the area of the hysteresis loop. This result indicates a decrease of micro/mesopore volume, which can be confirmed by the pore size distribution given in Fig. 3b. The mesopore size distribution curves indicate that the sizes of meso/macropores decrease due to the partial filling of SnO_2 NPs. A new peak appears between 4 and 9 nm, arising from the stacked pores among SnO_2 NPs dispersed in the pores or on the surface of PSCC, which is consistent with the HRTEM image (Fig. 2f). The meso/macropore size distribution and the hysteresis loop in the adsorption–desorption isotherm suggest that these interconnected pores are still open. The remaining porosity and the produced mesopores are beneficial for fast ion transport/electrolyte infiltration and provide space for

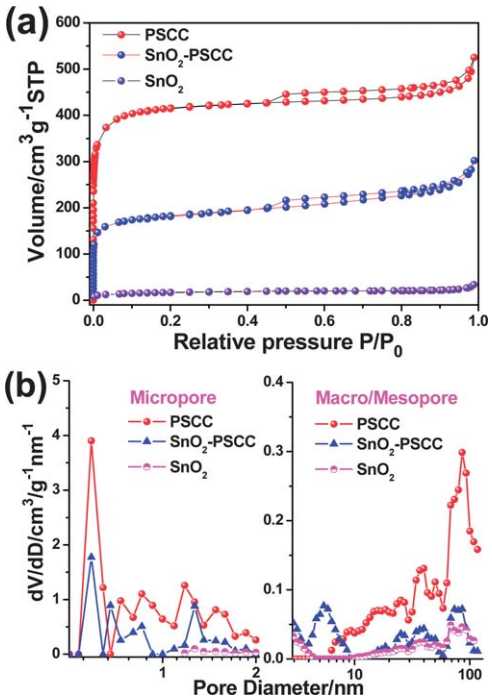

Fig. 3 (a) Nitrogen adsorption–desorption isotherms of the PSCC, SnO_2–PSCC hybrid and SnO_2. (b) Micropore-size and meso/macropore-size distributions of the PSCC, SnO_2–PSCC hybrid and SnO_2.

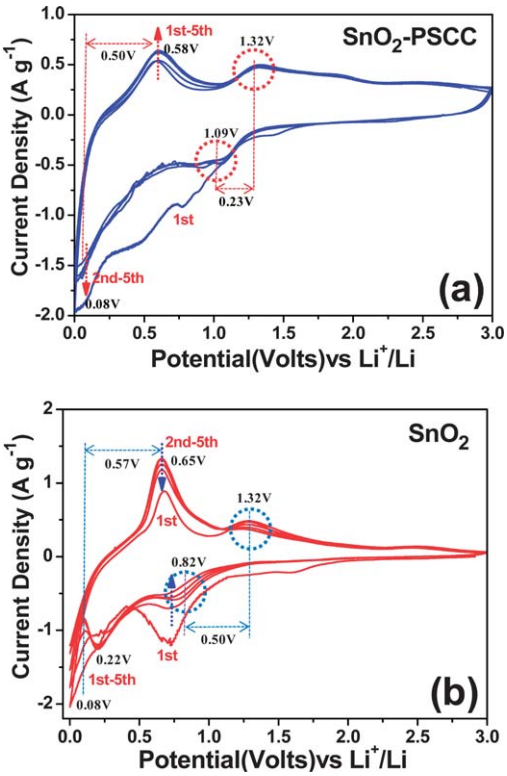

Fig. 4 CV curves of the (a) SnO_2–PSCC hybrid and (b) SnO_2 measured in the voltage range of 0.001 to 3.0 V (*vs.* Li^+/Li) at a scan rate of 0.5 mV s^{-1}.

accommodating the volume expansion of SnO_2 NPs during alloying/de-alloying processes.

To understand the effects of high active surface area, nano-size SnO_2 and porous nanostructures in improving the electrochemical properties of the hybrid, CV measurements were carried out to identify the electrochemical reactions during cycling. Fig. 4 shows the CVs of the SnO_2–PSCC hybrid and SnO_2 for the first five cycles at a scan rate of 0.5 mV s^{-1} in the potential window of 0.001 to 3 V. In the first cycle, as shown in Fig. 4a, reduction peaks at around 0.78 and 0.48 V are observed in the cathodic scan, which can be attributed to the formation of a solid electrolyte interphase (SEI) layer (eqn (1)) in SnO_2 and PSCC, and the peak at around 0.78 V may also be ascribed to the reduction of SnO_2 to Sn and the formation of Li_2O (eqn (2)).[9,18,31] These peaks disappear in the second cycle, suggesting the formation of a stable SEI layer. The peak of reaction (2) shifts from 0.78 to 1.09 V where it remains constant in the following cycles, which can be ascribed to improved kinetics. The other two inconspicuous peaks located around 0.08 and 0.01 V can be assigned to lithium alloying with Sn to form Li_xSn (eqn (3)) and lithium aggregation in micropores.[25,26,32] Three oxidation peaks appearing at around 0.19, 0.58 and 1.32 V correspond to lithium extraction from micropores, de-alloying of Li_xSn (eqn (3)) and the partially reversible reaction of Sn to SnO_2 (eqn (2)), respectively.[16,25] Eqn (2) is normally regarded as an irreversible reaction causing capacity loss,[12,22] while in this case the peak (1.32 V) remains stable for five cycles, indicating its partial reversibility. The oxidation peak at 0.58 V increases in the 2nd cycle and remains unchanged from the 3rd cycle, indicating an activation process in the initial electrochemical reactions. The CV characteristic of SnO_2 is shown in Fig. 4b. A broad peak at 0.75 V related to the formation of a SEI layer which can be seen up to the 5th cycle, indicating an irreversible reaction. The peaks at 0.82 and 1.32 V corresponding to eqn (2) monotonically decrease in the cycling process, implying its irreversibility which is different from the SnO_2–PSCC hybrid. The Li–Sn alloying reaction at 0.08 V shows a shift to 0.22 V after the 2nd cycle, indicating a decrease in the lithium content of the alloy, which is consistent with the decrease in the de-alloying peak at 0.65 V. Meanwhile, the two pairs of redox peaks of the SnO_2–PSCC hybrid can be clearly distinguished at 1.09/1.32 V and 0.08/0.58 V with a peak potential difference of 0.23 and 0.50 V, and these are lower than those of SnO_2 (0.50 and 0.57 V). These results indicate improved electrode reaction kinetics by the incorporation of highly conductive PSCC which is a key factor for obtaining high rate capability.

$$Li^+ + e^- + \text{electrolyte} \rightarrow \text{SEI (Li)} \quad (1)$$

$$SnO_2 + 4Li^+ + 4e^- \rightarrow Sn + 2Li_2O \quad (2)$$

$$Sn + xLi^+ + xe^- \leftrightarrow Li_xSn\ (0 \le x \le 4.4) \quad (3)$$

To determine whether the SnO_2–PSCC hybrid could improve the transfer kinetics of electrons and ions, EIS measurements were carried out, as shown in Fig. 5. The Nyquist plots of the SnO_2–PSCC hybrid and SnO_2 electrodes are nearly similar with a typical semicircle in the high-medium frequency region and an

inclined line in the low frequency region. The Nyquist plots were fitted by an appropriate electric equivalent circuit[30,33] (inset of Fig. 5) to obtain their kinetic parameters as given in Table 1. Here R_e is the ohmic resistance of the electrolyte and cell components, R_{ct} the charge-transfer resistance, R_{sf} the surface film resistance, CPE_i (sf, double layer (dl)) a constant phase element, Z_w the Warburg impedance, and C_{int} the intercalation capacitance. The single semicircle in the high/medium frequency can be ascribed to the combination of a surface film and charge-transfer resistances $R_{(sf+ct)}$.[33] According to the fitting results, the value of R_e is ~3.9 Ω for the two samples, indicating that the cells were properly fabricated and tested in the same condition. Importantly, the $R_{(sf+ct)}$ (90.2 Ω) for the SnO_2–PSCC hybrid is much smaller than that of SnO_2 with a value of 220.3 Ω, and the exchange current density ($i_0 = RT/nFR_{ct}$) of the SnO_2–PSCC hybrid is twice that of SnO_2, implying improved electron/ion transfer kinetics and electroactivity with respect to lithium storage.

Fig. 6 shows the discharge–charge curves of the SnO_2–PSCC hybrid and SnO_2 at a current density of 50 mA g^{-1}. The SnO_2–PSCC hybrid shows a first discharge capacity of 2012 mA h g^{-1} with high reversible capacity of 1256 mA h g^{-1}, which is among the highest values reported for SnO_2-based anode materials.[7–10,34–38] The plateau in the voltage region of 1.0–0.8 V *versus* Li^+/Li in the discharge curves can be ascribed to the reduction of SnO_2 to Sn and the formation of the SEI film (Fig. 6a).[31,39] There are two obvious stages (at 1.3 and 0.6 V from 1st to 30th) in the charge curves related to the de-alloying reaction (eqn (3)) and reversible oxidation of Sn to SnO_2 (eqn (2)). In contrast, the plateau reduces obviously at 0.6 V and even disappears at 1.3 V for SnO_2 from 1st to 30th indicating the irreversible transition process (Fig. 6b). These results are also consistent with CV measurements. Moreover, the difference is obvious for the SnO_2–PSCC hybrid and SnO_2 below 0.1 V in the discharge curve and above 1.5 V in the charge curve, which is also displayed in the CV curves with distinguishable areas as well. The capacity of the SnO_2–PSCC hybrid in these regions is much higher than that of SnO_2, which is due to the reversible lithium storage in PSCC verified by our previous work.[26]

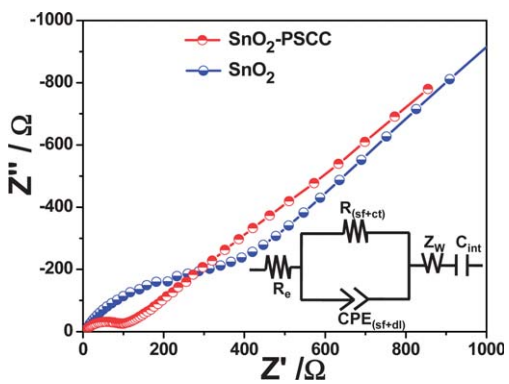

Fig. 5 Nyquist plots of the SnO_2–PSCC hybrid and SnO_2 electrodes measured in the frequency range from 10 mHz to 10 kHz with an alternating current amplitude of 10 mV. The impedance spectra were fitted by an equivalent circuit as shown in the inset.

Table 1 Impedance parameters calculated from equivalent circuits. i_0 was calculated according to $i_0 = RT/nFR_{ct}$, where R is the gas constant, T (K) the absolute temperature, n the number of transferred electrons, and F the Faraday constant

Samples	R_Ω (Ω)	R_{ct} (Ω)	$i_0 \times 10^{-4}$ (mA cm^{-2})
SnO_2–PSCC	3.9	90.2	2.87
SnO_2	4.0	220.3	1.17

Fig. 7a shows the cyclic performance and coulombic efficiency of the SnO_2–PSCC hybrid, PSCC and SnO_2 at a current density of 50 mA g^{-1}. The SnO_2–PSCC hybrid delivers a specific capacity of 1264 mA h g^{-1} after 30 cycles without any capacity loss showing high reversibility, similar to that of PSCC except for a much higher capacity. But SnO_2 delivers a reversible capacity of 1057 mA h g^{-1}, which quickly decreases to 392 mA h g^{-1}, equivalent to only 37% retention of the first capacity after 30 cycles. This is due to the large stress in agglomerated SnO_2 NPs that are not confined by the PSCC that deteriorates the electrode structure. Besides, the coulombic efficiency of the SnO_2–PSCC hybrid is above 97% after the initial two cycles (63% and 94%) and is more stable than that of the SnO_2. The large reversible capacity obtained is considered to be due to the synergistic effects of lithium storage in micropores and the highly reversible reactions of eqn (2) and (3). The SnO_2–PSCC shows a high surface area with large electrode–electrolyte interface for facilitating rapid charge-transfer reactions,[40] which enables complete reactions to promote the access of high reversible capacity.

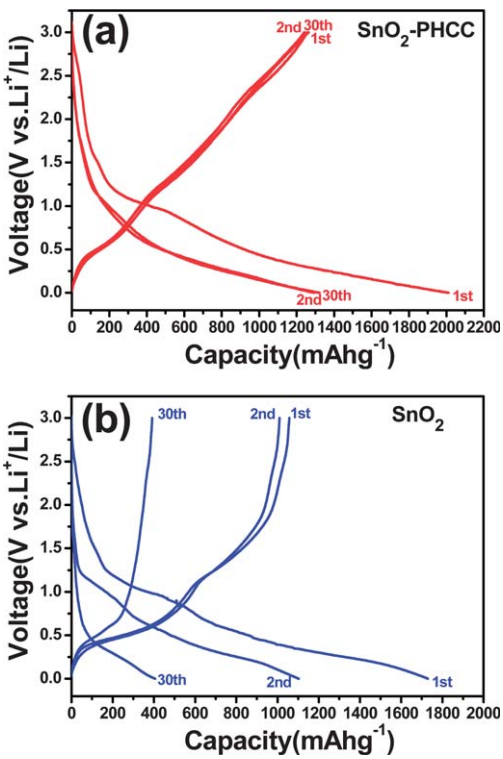

Fig. 6 The 1st, 2nd and 30th discharge–charge profiles of (a) the SnO_2–PSCC hybrid and (b) SnO_2 at a current density of 50 mA g^{-1}.

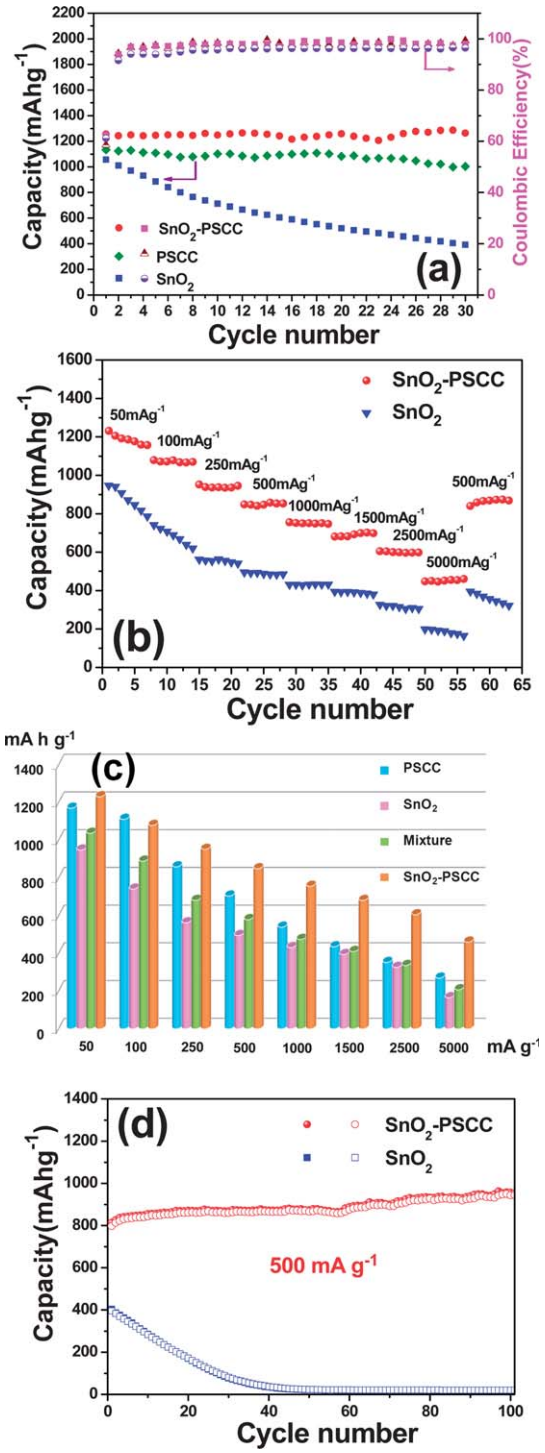

Fig. 7 (a) Cyclic performance and coulombic efficiency of the SnO_2–PSCC hybrid, PSCC and SnO_2 at a current density of 50 mA g^{-1} for 30 cycles. Pink symbol, coulombic efficiency for the SnO_2–PSCC hybrid; brown symbol, coulombic efficiency for the PSCC hybrid; purple symbol, coulombic efficiency for the SnO_2. (b) Rate performance of the SnO_2–PSCC hybrid and SnO_2 at different current densities. (c) The first reversible specific capacity of the PSCC, SnO_2, SnO_2–PSCC hybrid, and the calculated specific capacity of the SnO_2–PSCC hybrid based on the rule of mixture, at different current densities. (d) Cyclic performance of the SnO_2–PSCC hybrid and SnO_2 at a current density of 500 mA g^{-1} for 100 cycles. Solid symbols, discharge; hollow symbols, charge.

The SnO_2–PSCC hybrid also exhibits high rate capability, as shown in Fig. 7b. It delivers a reversible capacity of *ca.* 1200 mA h g^{-1} at a current of 50 mA g^{-1}. Upon increasing the current density to 500 and 5000 mA g^{-1} (6.4 C, 1 C = 780 mA h g^{-1}), the specific capacity of the hybrid remains at 860 and 460 mA h g^{-1}, demonstrating a magnificent high-rate performance. These values are remarkably higher than those for SnO_2 (only 485 and 165 mA h g^{-1}). Moreover, when the cycling current is restored to 500 mA g^{-1}, the hybrid electrode recovers its original capacity, implying that the structure of the electrode remains stable even under the high rate cycling. In contrast, the SnO_2 is not restored and exhibits a decreasing trend. The first reversible capacities of the SnO_2–PSCC hybrid at all the current rates are much higher than the theoretical value of the total sum of the individual capacity of SnO_2 (60 wt%) and PSCC (40 wt%), indicating a synergistic effect between these two components (Fig. 7c). This suggests that the high electrical conductivity, hierarchical porosity and confinement arising from the PSCC matrix are beneficial for improving reaction kinetics of the lithiation–delithiation of SnO_2. More significantly, the SnO_2–PSCC hybrid exhibits excellent cyclic performance which is the main problem holding back the implementation of SnO_2 in LIBs. The long cyclic stability of the samples was investigated after the high-rate capability test, as shown in Fig. 7d. It is surprising that even after suffering from the harsh conditions at various current densities after more than 60 cycles, the SnO_2–PSCC hybrid still shows a high stability with a specific capacity of 940 mA h g^{-1} in the following 100 cycles. The coulombic efficiency during cycling is close to 100%. A small increase in capacity can also be observed, which is attributed to the reversible growth of a polymeric gel-like film resulting from kinetically activated electrolyte degradation.[41,42] On the contrary, the capacity of SnO_2 decreases monotonically with cycling and decreases to zero after 50 cycles, indicating a poor cyclic stability, which is due to the large volume expansion/contraction and severe particle aggregation on lithiation and delithiation, leading to pulverization of the active material.

To further elucidate the improved electrochemical performance of the hybrid, the cells of the SnO_2–PSCC hybrid and SnO_2 after 30 cycles of charging–discharging tests were disassembled and the electrodes were taken out and observed under SEM and TEM. As shown in Fig. S3a,† no obvious change can be observed for SnO_2–PSCC hybrid and the porous spherical morphology was still preserved. The uniform SnO_2 NPs were clearly embedded in PSCC without agglomeration (Fig. S3c†), demonstrating the structure integrity of the hybrid and the confinement effect from PSCC during cycles. In contrast, particle agglomeration can be clearly seen in SEM and TEM images of the SnO_2 electrode (Fig. S3b and d†), indicating the severe aggregation of SnO_2 during cycling that leads to the fast capacity fading. The high rate performance and remarkably improved cyclic stability of the SnO_2–PSCC hybrid can be attributed to the uniform dispersion of SnO_2 NPs and the additional voids formed between them that shorten Li^+ diffusion length and increase the lithiation reactivity of SnO_2. Moreover, the meso/macropores accommodate volume changes and prevent the agglomeration of SnO_2 NPs, and the NPs

sustain a lower absolute volume change during the discharge–charge processes.

4 Conclusion

It is found that the SnO_2–PSCC hybrid has a high reversible lithiation capacity and good cyclic stability. The unique structure of the SnO_2–PSCC hybrid includes preserved inter-connected pores, homogeneously dispersed and confined SnO_2 NPs, and a highly electrically conductive PSCC. These characteristics provide favorable transport kinetics for both ions and electrons, and improved reaction kinetics for reversible lithiation–delithiation. The improved kinetics of the SnO_2–PSCC hybrid enables the achievement of high reversible capacity, excellent rate capability and outstanding cyclability, indicating its potential use as an anode material for high energy and high power LIBs.

Acknowledgements

This work was supported by Ministry of Science and Technology of China (no. 2011CB932604), National Science Foundation of China (nos 50921004 and 51172239) and Chinese Academy of Sciences.

Notes and references

1 J. M. Tarascon and M. Armand, *Nature*, 2001, **414**, 359–367.
2 M. Armand and J. M. Tarascon, *Nature*, 2008, **451**, 652–657.
3 P. G. Bruce, B. Scrosati and J. M. Tarascon, *Angew. Chem., Int. Ed.*, 2008, **47**, 2930–2946.
4 N. A. Kaskhedikar and J. Maier, *Adv. Mater.*, 2009, **21**, 2664–2680.
5 C. Liu, F. Li, L.-P. Ma and H.-M. Cheng, *Adv. Mater.*, 2010, **22**, E28–E62.
6 Y. Idota, T. Kubota, A. Matsufuji, Y. Maekawa and T. Miyasaka, *Science*, 1997, **276**, 1395–1397.
7 Y. Yu, C. H. Chen and Y. Shi, *Adv. Mater.*, 2007, **19**, 993–997.
8 W. M. Zhang, J. S. Hu, Y. G. Guo, S. F. Zheng, L. S. Zhong, W. G. Song and L. J. Wan, *Adv. Mater.*, 2008, **20**, 1160–1165.
9 X. W. Lou, C. M. Li and L. A. Archer, *Adv. Mater.*, 2009, **21**, 2536–2539.
10 C. M. Park, J. H. Kim, H. Kim and H. J. Sohn, *Chem. Soc. Rev.*, 2010, **39**, 3115–3141.
11 Y. Wang, F. B. Su, J. Y. Lee and X. S. Zhao, *Chem. Mater.*, 2006, **18**, 1347–1353.
12 L. Zou, L. Gan, R. T. Lv, M. X. Wang, Z. H. Huang, F. Y. Kang and W. C. Shen, *Carbon*, 2011, **49**, 89–95.
13 Y. Li, S. M. Zhu, Q. L. Liu, J. J. Gu, Z. P. Guo, Z. X. Chen, C. L. Feng, D. Zhang and W. J. Moon, *J. Mater. Chem.*, 2012, **22**, 2766–2773.
14 Y. Chen, Q. Z. Huang, J. Wang, Q. Wang and J. M. Xue, *J. Mater. Chem.*, 2011, **21**, 17448–17453.
15 X. W. Lou, Y. Wang, C. L. Yuan, J. Y. Lee and L. A. Archer, *Adv. Mater.*, 2006, **18**, 2325–2329.
16 R. Demir-Cakan, Y. S. Hu, M. Antonietti, J. Maier and M. M. Titirici, *Chem. Mater.*, 2008, **20**, 1227–1229.
17 D. Deng and J. Y. Lee, *Chem. Mater.*, 2008, **20**, 1841–1846.
18 H. Wang, Y. Wu, Y. Bai, W. Zhou, Y. An, J. Li and L. Guo, *J. Mater. Chem.*, 2011, **21**, 10189–10194.
19 Z. Wang, D. Luan, F. Y. C. Boey and X. W. Lou, *J. Am. Chem. Soc.*, 2011, **133**, 4738–4741.
20 J. Fan, T. Wang, C. Z. Yu, B. Tu, Z. Y. Jiang and D. Y. Zhao, *Adv. Mater.*, 2004, **16**, 1432–1436.
21 F. B. Su, X. S. Zhao, Y. Wang, J. H. Zeng, Z. C. Zhou and J. Y. Lee, *J. Phys. Chem. B*, 2005, **109**, 20200–20206.
22 Z. H. Wen, Q. Wang, Q. Zhang and J. H. Li, *Adv. Funct. Mater.*, 2007, **17**, 2772–2778.
23 H. X. Zhang, C. Feng, Y. C. Zhai, K. L. Jiang, Q. Q. Li and S. S. Fan, *Adv. Mater.*, 2009, **21**, 2299–2304.
24 S. M. Paek, E. Yoo and I. Honma, *Nano Lett.*, 2009, **9**, 72–75.
25 J. Yao, X. P. Shen, B. Wang, H. K. Liu and G. X. Wang, *Electrochem. Commun.*, 2009, **11**, 1849–1852.
26 G. M. Zhou, D. W. Wang, X. Y. Shan, N. Li, F. Li and H.-M. Cheng, *J. Mater. Chem.*, 2012, **22**, 11252–11256.
27 G. M. An, N. Na, X. R. Zhang, Z. J. Miao, S. D. Miao, K. L. Ding and Z. M. Liu, *Nanotechnology*, 2007, **18**, 435707.
28 S. D. Gardner, C. S. K. Singamsetty, G. L. Booth, G. R. He and C. U. Pittman, *Carbon*, 1995, **33**, 587–595.
29 W. Lv, D. M. Tang, Y. B. He, C. H. You, Z. Q. Shi, X. C. Chen, C. M. Chen, P. X. Hou, C. Liu and Q. H. Yang, *ACS Nano*, 2009, **3**, 3730–3736.
30 G. M. Zhou, D.-W. Wang, L.-C. Yin, N. Li, F. Li and H.-M. Cheng, *ACS Nano*, 2012, **6**, 3214–3223.
31 P. Meduri, E. Clark, E. Dayalan, G. U. Sumanasekera and M. K. Sunkara, *Energy Environ. Sci.*, 2011, **4**, 1695–1699.
32 Q. Wang, H. Li, L. Q. Chen and X. J. Huang, *Carbon*, 2001, **39**, 2211–2214.
33 M. V. Reddy, T. Yu, C. H. Sow, Z. X. Shen, C. T. Lim, G. V. S. Rao and B. V. R. Chowdari, *Adv. Funct. Mater.*, 2007, **17**, 2792–2799.
34 S. J. Ding, J. S. Chen, G. G. Qi, X. N. Duan, Z. Y. Wang, E. P. Giannelis, L. A. Archer and X. W. Lou, *J. Am. Chem. Soc.*, 2011, **133**, 21–23.
35 P. Meduri, C. Pendyala, V. Kumar, G. U. Sumanasekera and M. K. Sunkara, *Nano Lett.*, 2009, **9**, 612–616.
36 J. X. Li, Y. Zhao, N. Wang and L. H. Guan, *Chem. Commun.*, 2011, **47**, 5238–5240.
37 D. Deng, M. G. Kim, J. Y. Lee and J. Cho, *Energy Environ. Sci.*, 2009, **2**, 818–837.
38 X. Wang, X. Q. Cao, L. Bourgeois, H. Guan, S. M. Chen, Y. T. Zhong, D. M. Tang, H. Q. Li, T. Y. Zhai, L. Li, Y. Bando and D. Golberg, *Adv. Funct. Mater.*, 2012, **22**, 2682–2690.
39 J. Li, Y. Zhao, N. Wang and L. Guan, *Chem. Commun.*, 2011, **47**, 5238–5240.
40 S. B. Yang, X. L. Feng, L. J. Zhi, Q. A. Cao, J. Maier and K. Mullen, *Adv. Mater.*, 2010, **22**, 838–842.
41 S. Laruelle, S. Grugeon, P. Poizot, M. Dolle, L. Dupont and J. M. Tarascon, *J. Electrochem. Soc.*, 2002, **149**, A627–A634.
42 G. M. Zhou, D. W. Wang, F. Li, L. L. Zhang, N. Li, Z. S. Wu, L. Wen, G. Q. Lu and H. M. Cheng, *Chem. Mater.*, 2010, **22**, 5306–5313.

